RESEARCH ARTICLE

# Ultra-fast X-ray particle velocimetry measurements within an abrasive water jet

**R. Balz · R. Mokso · C. Narayanan ·
D. A. Weiss · K. C. Heiniger**

**Abstract** Ultra-fast X-ray velocimetry measurements were taken to measure velocities and spatial positions of individual abrasive particles within the solid–liquid–gaseous three-phase flow of a high-pressure injection method–based abrasive water jet (AWJ). A synchrotron X-ray source provided sufficient photon flux to take double-frame images of the AWJ with an inter-frame time interval of 5 μs. Abrasive particles with a Sauter mean diameter of 265.5 μm were detected by a scintillator optically coupled to a gated image intensifier and a high-speed camera running at a frame rate of 11,250 Hz. A commercially available particle tracking velocimetry software was used to process the acquired images and evaluate the spatial positions and velocities of abrasive particles as a function of water pressure and abrasive mass flow. The acquired data show a Gaussian radial distribution of abrasive particles within the AWJ and an almost uniform mean axial velocity, irrespective of water jet velocity and abrasive flow rates. These results are useful to validate theoretical models for the momentum/energy transfer in AWJ, to provide input for abrasion/erosion models, to further understand and advance the AWJ process, and to develop new process opportunities such as AWJ milling.

R. Balz · C. Narayanan · D. A. Weiss (✉) · K. C. Heiniger
Institute of Thermal and Fluid Engineering, University of
Applied Sciences Northwestern Switzerland, Klosterzelgstrasse
2, 5210 Windisch, Switzerland
e-mail: daniel.weiss@fhnw.ch

K. C. Heiniger
e-mail: kurt.heiniger@fhnw.ch

R. Mokso
Swiss Light Source, Paul Scherrer Institut, 5232 Villigen,
Switzerland

## List of symbols

| | |
|---|---|
| $x$ | $x$-coordinate |
| $y$ | $y$-coordinate |
| $z$ | $z$-coordinate |
| $n$ | Constant (0.1368 at 25° C) |
| $L$ | Constant (300 MPa) |
| $v$ | Abrasive particle mean axial velocity |
| $v_i$ | Isentropic velocity of AWJ |
| $\rho_w$ | Density of water at $\Delta p = 0$ |
| $\Delta p$ | Mean relative water pressure |
| $v_x$ | Abrasive particle velocity component in $x$-direction |
| $v_z$ | Abrasive particle velocity component in $z$-direction |
| $d_{[3,2]}$ | Sauter mean diameter of the abrasive particles |
| $d_{[v,0.1]}$ | 10 % of the volume of the abrasive particles is below this diameter |
| $d_{[v,0.9]}$ | 90 % of the volume of the abrasive particles is below this diameter |
| $r_F$ | Focusing tube inner radius |
| $R_s^2$ | Coefficient of determination for spatial distribution Gauss fit |
| $R_v^2$ | Coefficient of determination for velocity distribution Gauss fit |
| $R_p^2$ | Coefficient of determination for velocity profile polynomial fit |
| $f_s(x)$ | Gauss function for spatial distribution fit |
| $f_v(x)$ | Gauss function for velocity distribution fit |
| $f_p(x)$ | Polynomial function for velocity profile fit |
| $v_{t,\max}$ | Theoretical maximal axial velocity of abrasive particles |
| $\dot{m}_{w,\text{in}}$ | Inlet water jet mass flow rate |
| $\dot{m}_{w,\text{out}}$ | Outlet water jet mass flow rate |
| $\dot{m}_{a,\text{out}}$ | Outlet abrasive particle mass flow rate |
| $\dot{m}_a$ | Abrasive particle mass flow rate |
| $\dot{m}_w$ | Water jet mass flow rate |

# 1 Introduction

High-energy abrasive water jet (AWJ) cutting, based on the injection method, is a widespread industrial process for a variety of both ductile and brittle materials. The AWJ cutting process has a major advantage over other manufacturing processes, for example, laser cutting, since there is no interference with the material's internal structure. The injection method–based AWJ involves a three-phase flow mixture of water (liquid), air (gas), and abrasive particles (solid). It is driven by a high-speed water jet formed by leading water with a pressure of several hundred MPa through a small nozzle with an orifice of about 0.05–0.5 mm in diameter. The resulting water jet reaches velocities of several hundred meters per second and generates low pressure accelerating the surrounding air in the so-called mixing chamber, which allows for suction of abrasive particles and air. The abrasive particles are typically garnet, with a representative diameter between 0.05 and 0.5 mm. The abrasive particles and air are accelerated by momentum exchange with the water jet in the so-called focusing tube, which has a diameter between 0.3 and 1.5 mm. The focusing tube is usually made of hard materials such as carbide to minimize wear by the abrasive particles. Figure 1 shows a sketch of a typical cutting head of a commercial AWJ system.
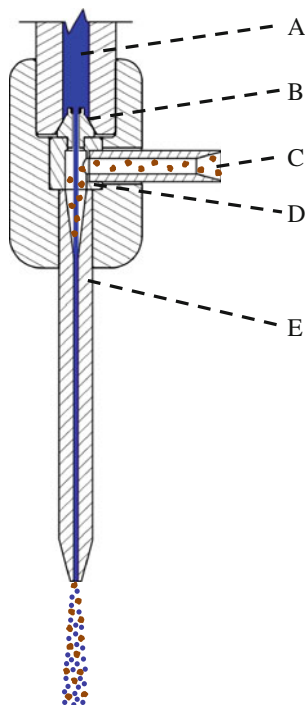


**Fig. 1** Abrasive water jet (AWJ) cutting head. *A* high pressurized water, *B* orifice, *C* abrasive particles and air inlet, *D* mixing chamber, *E* focusing tube

Since almost all of the abrasion from the AWJ is due to the abrasive particles, accurate knowledge of the abrasive particles' spatial distribution within the AWJ is needed, if the AWJ cutting process is to be further understood and improved in performance, and if new process opportunities such as AWJ milling are to be developed.

Previous studies used different measurement techniques to estimate the abrasive particle velocity and mass distribution. The studies can be classified into those using optical techniques and those which do not. The non-optical methods include flow separation by a diamond washer (Geskin et al. 1989), force measurements (Li et al. 1989), and rotary disk measurements, where fast rotating disks separate the AWJ, allowing calculation of the velocity via erosion displacements (Isobe et al. 1988). Inductive measurements used coils and magnetic tracer particles to estimate the particle velocity within the AWJ (Swanson et al. 1987). The main problem of the measurement method related to the varying velocity results for different mass ratios of tracer and abrasive particles, since the tracer material had higher densities. Scanning X-ray densitometry was used to measure the mass distribution in the AWJ by measuring the absorption of the X-ray through the AWJ (Neusen et al. 1990). These results were only qualitative and could not give the desired quantitative results. The common factor in all these measurements is the lack of spatial information for both, velocity and particle distribution.

Optical methods include laser Doppler anemometry (LDA) and laser transit velocimetry (LTV). Neusen et al. (1994) measured the average velocity of the AWJ with LDA. Chen and Geskin (1997) used LTV to estimate the kinetic energy profile of the AWJ. The measurements mentioned above have to some extent a spatial resolution but cannot differentiate between water droplets and abrasive particles. High-speed imaging was used by Claude et al. (1998) and Roth et al. (2005) to measure the average velocity of the AWJ. These measurements had no spatial resolution of the abrasive particles either.

Balz and Heiniger (2011) improved the measurement technique introduced by Roth et al. (2005) to measure, not only the spatial distribution, but also the spatial velocity distribution of individual abrasive particles by stereoscopic imaging. Fluorescent-dyed abrasive particles and long-pass filters in front of the cameras that block the laser light have been used, to make only the dyed abrasive particles visible. Although the desired results were obtained, there were several problems such as the disintegration of the abrasive particles during the acceleration process, and the fact that the laser beam did not fully penetrate the AWJ due to optical interactions. This measurement technique also had a limited acquisition frequency due to the double-pulsed laser used. In spite of these disadvantages, the 3D laser-induced fluorescence measurements technique gives the full positional information of the detected abrasive

particles, which is not possible with the other methods presented above, since stereoscopic information is missing.

The previous studies showed that the most success in detecting single abrasive particles velocity and spatial position was feasible with optical methods since they are noninvasive, allow very short exposure times, and have enough spatial resolution to detect the abrasive particles position within the AWJ. However, optical measurement techniques using laser light in the visible range of the spectrum are limited because of the interactions with the free surfaces of water droplets and air bubbles in the three-phase flow. The experiments also require changes in the AWJ process, such as the experiments performed by Roth et al. (2005) and Balz and Heiniger (2011), where fluorescent-dyed abrasive particles had to be used.

X-rays provide an alternative way because photons with wavelengths in the X-ray spectrum circumvent some of the light scattering difficulties. X-ray reflection and refraction angles are small, and X-rays travel in straight lines to allow transmission imaging geometry to be used. The interaction of X-rays with water, abrasive particles, and air is weak; thus, volumetric measurements are possible while still providing satisfactory contrast between each element of the multi-phase system.

Most of the existing studies to measure multiphase flow with X-rays examined fuel sprays. Ramirez et al. (2009) performed X-ray measurements on high-pressure fuel sprays, but used an avalanche photodiode with a very fast response of 5 ns, which would not permit the spatial resolution of abrasive particles. Wang et al. (2008) used X-ray phase contrast imaging to also analyze fuel sprays. Although the spray velocities of 60 m/s are very low compared with the AWJ application, they worked with an interframe time of 3.68 μs and exposure time of 472 ns. They used double exposures with subsequent autocorrelation techniques to extract the velocities. Lee and Kim (2005) used an X-ray particle tracking velocimetry technique to simultaneously measure velocities and sizes of micro-bubbles in a fluid. The micro-bubbles had diameters between 10 and 60 μm, but very low speeds; the time between two frames of the CCD camera was set to 40 ms. Multi-fluid phase interactions have been observed by Hansson et al. (2009), who developed a synchronized high-speed visualization by digital cinematography and X-ray radiography to visualize the process of droplet explosion. They used a 320 keV X-ray tube and had a spatial resolution of 0.126 mm/pixel, and the droplet velocity reached 0.6 m/s.

The common feature among most of these measurements is that they used an X-ray source, a high-resolution camera, and a scintillator. Bieberle et al. (2009) used an X-ray detector arc around a pipe to visualize and measure a gas–liquid two-phase flow. A linear electron beam scan has been used to produce radiographic views. Although very high temporal resolution (sampling rate of 1 MHz) could

be achieved, the spatial resolution is limited to 1 mm. As the work presented by Bieberle et al. (2009) made use of an X-ray computer tomography technique, it cannot be directly compared to the radiographic techniques.

In the present work, high temporal and spatial resolution have been combined to capture in a continuous manner particle spatial distribution and velocity fields in an AWJ. The method we present does not require a special operation mode of the synchrotron X-ray source (unlike in Wang et al. 2008) lending it more flexibility and easier implementation. The high velocities of the abrasive particles require a high photon-flux X-ray source to perform image acquisition with exposures within the range of microseconds, to keep the displacement of the abrasive particles minimal. For such short exposure times, no conventional X-ray source (with rotating anode) could be used, due to insufficient photon intensities. Third-generation synchrotron light sources such as the Swiss Light Source (SLS) at the Paul Scherrer Institute in Villigen, Switzerland, are characterized by several orders of magnitude higher brightness (photon flux per unit area, angle, and time) and are therefore suitable for ultra-fast high spatial resolution measurements. The beamline for tomographic microscopy and coherent radiology experiments (TOMCAT) produces a photon flux of more than $10^{14}$/s, which allows exposure times of the order of microseconds.

## 2 Experiment

### 2.1 Optical setup

A particle tracking shadowgraphy, that is, an optical measurement technique, was adapted to the continuous X-ray source at the SLS. Polychromatic photons resulting from the superbending magnet of the TOMCAT beamline were used directly without a monochromator. The broadband spectrum of this probe was filtered only spatially in the detector plane by using a narrow horizontal window, where high-energy X-rays prevail as a consequence of the Gaussian source spectral distribution. A 10 bit monochrome CMOS high-speed camera (HSC) with a particle image velocimetry mode allowed fast-frame transfer and a high frame rate. A gated image intensifier (IRO) based on a micro-channel-plate allowed to control the exposure time, which had to be very short since the X-ray source is continuous, and therefore, the abrasive particles would smear out by leaving their trajectories if they were exposed too long. In addition, the IRO allowed intensifying the incident photons from the scintillator.

A visible light relay optics–based macroscope coupled to a 300 μm thin LuAG:Ce scintillator with a decay time of about 70 ns was mounted in front of the IRO and the HSC. A mechanical trigger with a frequency of 20 Hz was used
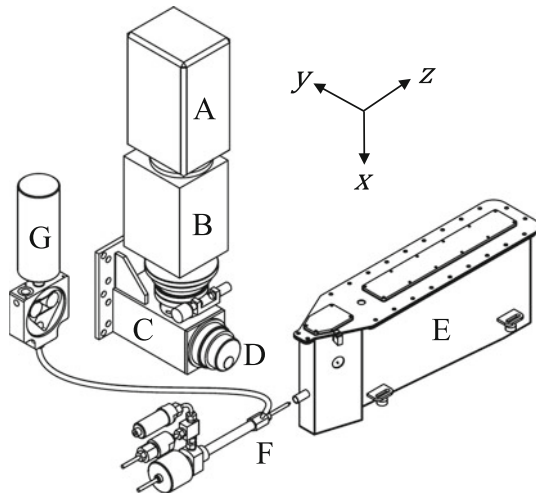
**Fig. 2** Optical setup. *A* high-speed camera (HSC), *B* gated image intensifier (IRO), *C* macroscope, *D* scintillator, *E* catcher, *F* abrasive water jet (AWJ) cutting head with high-pressure sensor and inline 35 μm filter, *G* abrasive dosing system

to pulse the X-ray beam for reasons of durability of the scintillator (see Fig. 2).

The frame rate of the HSC was set to the maximum value of 11,250 Hz. The region of interest (ROI) of the HSC's CMOS sensor was set to 2.0 mm × 18.0 mm. With this frame rate, the HSC's internal memory allowed taking 24,576 double images with an inter-frame time of 5 μs within 2.185 s, excluding the pauses in acquisition during the times when the mechanical shutter was closed. The transfer time of the images acquired from the HSC's memory was slow; taking about 35 min. The resulting resolution of the optical setup was 17.2 μm/pixel.

The detector system was installed at a distance of 25 m from the X-ray source. A distance of 0.17 m between the AWJ focusing tube and the detector scintillator screen allowed for interference of the X-rays transversing the sample and resulted in the enhancement of the intensity contrast in the images.

### 2.2 Experimental setup

The AWJ cutting head was mounted horizontally to optimize the field of view to the X-ray beam at the TOMCAT beam line. Since usual AWJ applications work vertically or just slightly tilted with respect to the vertical axis, a special catcher had to be constructed to dissipate the horizontally aligned AWJ's energy and collect water and abrasive particles without any pollution. A commercial cutting head with an orifice diameter of 0.28 mm, a focusing tube of diameter 0.80 mm, and length 76 mm were used, together with size-classified garnet abrasive particles. The water pressure was measured by a high-pressure sensor at the AWJ cutting head inlet, and the abrasive mass flow was fed

to the AWJ cutting head with a commercial belt-driven dosing system, to guarantee exact known parameters. All systems had to be operated remotely, since the experimental hutch is completely shielded against the ionizing radiation. The abrasive particles had been classified by sieving with meshes 0.20 and 0.25 mm. A laser diffraction size measurement yielded diameters as a $d_{[3,2]}$ of 265.5 μm, a $d_{[v,0.1]}$ of 183.94 μm, and a $d_{[v,0.9]}$ of 420.5 μm.

The limited beam time scheduled at the TOMCAT beam line allowed the measurement of a total of 36 sets. 14 sets with different water pressures and abrasive mass flow rates, 6 sets with different angles between the abrasive and air inlet and one set with non-classified original mesh 80 garnet were measured and evaluated in our experiments.

The whole setup was aligned to the X-ray beam, so that the exit of the focusing tube was no more visible on the HSC. With this setup, the ROI extended from the end of the focusing tube over a distance of 18 mm in *z*-direction. Measurements within the focusing tube are not feasible because of the low transparency of the focusing tube's walls at energies below 40 keV.

The discharge coefficient of the 0.28 mm orifice used was measured before and after the experiment, to guarantee similar experimental conditions. The discharge coefficient was evaluated by measurements of the orifice diameter with a microscope, and the water mass flow was determined by means of a coriolis mass flow meter at about 25 MPa water pressure. The change of the discharge coefficient lies within the accuracy of measurement. Since the AWJ was running for only about 20 s for each set, the total cumulative time of running the AWJ for all measurements amounted to about 720 s. This short time guaranteed negligible changes of the AWJ regarding wear of the mixing chamber, the orifice, and the focusing tube, since the usual time of operation of the mixing chambers and focusing tubes used is usually more than 15 h.

### 2.3 Image processing and evaluation

The intensities of the images recorded contain information on the attenuation as well as phase shifting difference of the abrasive particles relative to the water column. In particular, the edges of the abrasive particles were enhanced due to the phase contrast content. Nevertheless, the noise content of the images was high because of the small photon statistics. The images were processed with a series of filters to prepare the input for the evaluation with commercial software. The output from this evaluation was the abrasive particle's position on both frames of each image. With this information and the inter-frame time known, the two velocity components $v_x$ and $v_z$ could be calculated.

The low contrast and granularity of the raw images required image processing to improve the algorithm's
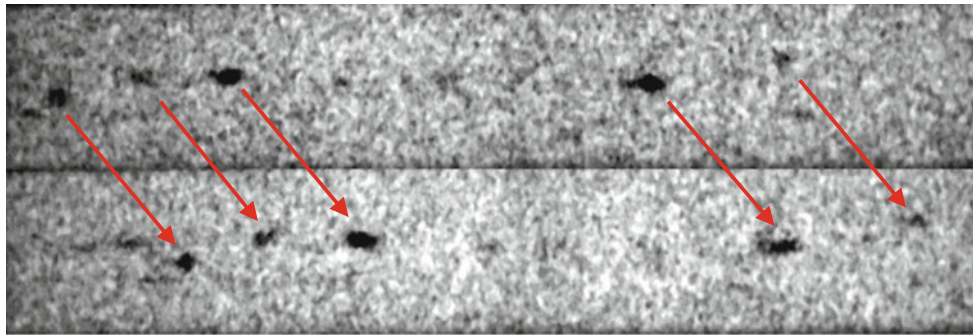
**Fig. 3** Image acquisitioned after background subtraction shows both frames pictured one above the other. The AWJ direction is from left to right. The *dark spots* indicate the abrasive particles

reliability to obtain the abrasive particle positions. The following image processing steps were applied to the raw images:

1. Background subtraction
2. Intensity correction
3. Median filter
4. Wiener filter
5. Threshold operation

The first step, the background subtraction, was necessary since the X-ray beam was not homogenous, and therefore, the center of the beam has the most intensity. Although background images without the AWJ had been measured, best results were performed by means of a moving average of ten images with the running AWJ. Intensity correction was used to improve the image contrast by mapping the intensity, so that one percent of the data were saturated at low and high intensities. The median filter reduced noise and preserved the edges in the images. Wiener filter further reduced noise by a pixel-wise adaptive method based on statistics estimated from a local neighborhood of each pixel (Lim 1990). The last step, threshold operation, suppressed all maxima in the image intensity whose values were less than the mean of all values in the image. This increased the surrounding pixels of an abrasive particle and therefore its visibility.

Figure 3 shows a double-frame image acquired after background subtraction. The two frames are shown one above the other and the arrows indicate the displacement of the abrasive particles detected, shown as dark spots. The images processed were evaluated with a particle tracking velocimetry algorithm by commercial software used for shadowgraphy imaging evaluation (Davis from LaVision GmbH).

# 3 Results

Together with the positions of all detected abrasive particles on both frames, the mean velocity, the velocity distribution, and the distribution of the abrasive particles within the AWJ were analyzed. The results of the 14 sets with various AWJ parameters are given in the "Appendix." Additionally, the abrasive particles were analyzed for changes in size distribution before and after the AWJ cutting process, to investigate the abrasive particle disintegration during the acceleration process.

## 3.1 Abrasive particle size distribution

The disintegration of the abrasive particles during the acceleration process is an important phenomenon occurring in AWJ operation, since the abrasive particle distribution changes significantly. The results shown here were obtained after the SLS experiment using a specially manufactured catcher that completely dissipates the abrasive particle kinetic energy by interaction with water. Therefore, no further disintegration of the abrasive particles took place in this series after the exit of the focusing tube. The collected abrasive particles were analyzed by a laser diffraction size instrument and compared with the original abrasive particles. Figure 4 shows the measurement results of the laser diffraction size instrument. The dashed line represents the used abrasive particles that have been collected after passing the AWJ cutting head with a mass flow of 4.17 g/s and a water pressure of 296.4 MPa.

Compared with the original charge of abrasive particles, the curve has shifted toward smaller abrasive particle sizes. For example, the percentage of 100 μm particles has increased significantly, which reflects the breakup of the abrasive particles. This observation is consistent with findings reported in literature (Hlavac et al. 1999).

## 3.2 Abrasive particle spatial distribution

Figure 5 shows the spatial distribution of 39′217 abrasive particles detected within the AWJ, where a water pressure of 91.0 MPa and a mass flow ratio of abrasive particles and water of 0.183 had been applied. The radial position of the
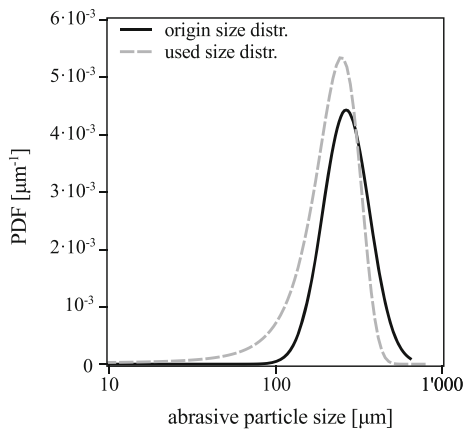
**Fig. 4** Abrasive particle size distribution before and after acceleration. The used size distribution shown was measured after passing the AWJ cutting head with a mass flow of 4.17 g/s and a water pressure of 296.4 MPa
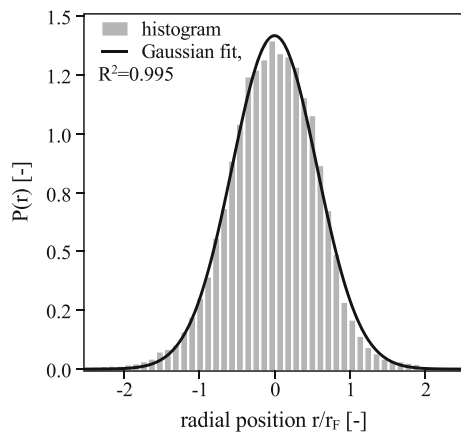


**Fig. 5** Abrasive particle distribution within the AWJ of 39,217 detected abrasive particles at a water pressure of 91.0 MPa and a mass flow ratio of 0.183

abrasive particles is scaled by the inner radius $r_F$ of the focusing tube. The data have also been fit by a Gaussian curve.

Note that the optical and experimental setup only allowed detecting two out of three components of the spatial coordinates and velocities of the abrasive particles. There is no information available on the position of the abrasive particles in $y$-direction, since the X-ray beam was aligned in this direction. Stereoscopic X-ray imaging would be required to evaluate the complete spatial information. Although no full spatial resolution could be realized, almost all abrasive particles can be considered as single events because of the high velocity of the water jet and the low mass flow ratio of abrasive particles and water. Particle–particle interactions and overlapping of abrasive particles are statistically insignificant and can be neglected at all. The positions of the abrasive particles were collected into bins for better visualization. The AWJ slightly spreads

downstream of the focusing tube due to disintegration. This effect is indicated in Fig. 5; the distribution of the abrasive particles exceeds the focusing tube inner diameter at the positions 1 and −1 on the abscissa of the plot. As the absolute radial velocity component of the abrasive particles is about 0–4 % of the axial velocity, it can be neglected since total momentum calculations have shown no significant difference.

### 3.3 Abrasive particle velocity distribution

Figure 6 shows a velocity distribution of 48′810 detected abrasive particles. The velocities $v$ are scaled by the isentropic velocity $v_i$ of the water jet behind the orifice. Measurements have been taken with a water pressure of 296.6 MPa and a mass flow ratio of abrasive particles and water of 0.208. The arithmetic mean axial velocity of the dataset shown is $435.1 \pm 65.1$ m/s. The isentropic velocity $v_i$ is calculated based on Bernoulli's law, complemented by a compressibility coefficient, which is derived from the water compressibility equation, as presented in Hashish (2003):

$$v_i = \psi \cdot \sqrt{\frac{2 \cdot \Delta p}{\rho_w}} \tag{1}$$

The compressibility coefficient $\psi$ is defined as

$$\psi = \sqrt{\frac{L}{\Delta p \cdot (1 - n)} \cdot \left[ \left(1 + \frac{\Delta p}{L}\right)^{1-n} - 1 \right]} \tag{2}$$

where the constant $L$ equals 300 MPa and $n$ equals 0.1368 at 25° C.

The histogram shown in Fig. 6 has been fit with a Gaussian function and shows good agreement, as the coefficient of determination $R^2$ is 0.998.
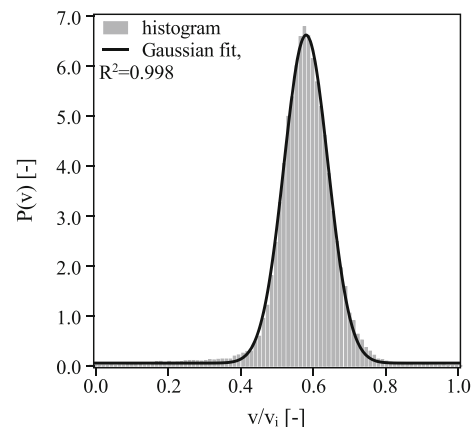


**Fig. 6** Abrasive particle velocity distribution of 48,810 detected abrasive particles at a water pressure of 296.6 MPa and a mass flow ratio of 0.208

The velocity distribution shown is dependent on the AWJ cutting head geometry and the abrasive particle sizes used, as well as on the water pressure and abrasive mass flow. Since the water jet disintegrates by the acceleration process of air (leads to wall shear), and since a shock occurs within the focusing tube upstream its exit (see Osman et al. (2004) for further details), the velocity ratio $v/v_i$ downstream the exit of the focusing tube cannot reach 1, even when no abrasive particles are involved. Strong abrasive particle size differences, turbulence fluctuations, and collisions with the focusing tube wall lead to the width of the velocity histogram. The axial velocity of individual abrasive particles in turn is dependent on the abrasive particle size: Small abrasive particles reach higher velocities after the given distance of acceleration within the focusing tube than bigger and therefore heavier abrasive particles, because of the mass dependent momentum exchange. The abrasive particle velocity distributions evaluated of all 14 sets acquired with different AWJ parameters are presented in Fig. 9 in the "Appendix".

### 3.4 Abrasive particle velocity profile within the AWJ

Figure 7 shows the spatial velocity distribution of the abrasive particles detected within the AWJ. The abrasive particles velocities were arithmetically averaged over defined bins. The error bars represent the standard deviation.

The averaged abrasive particle axial velocity, which is almost flat within the AWJ, was fit with a 3rd grade polynomial function with a coefficient of determination $R^2$ of 0.95. The shaded circle in the right bottom corner of Fig. 7 represents the Sauter mean diameter of the abrasive particles used. The diameter of abrasive particles is not small in comparison with the focusing tube diameter.
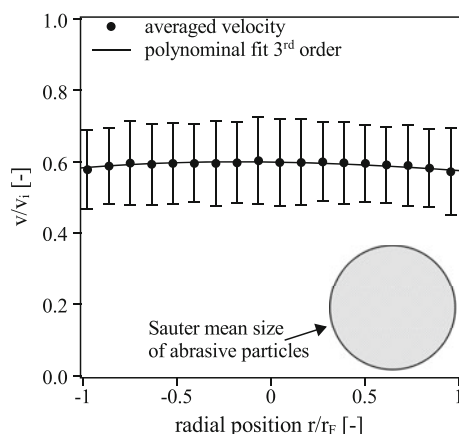
The limited spatial resolution and signal-to-noise ratio of the images acquired were the main sources of uncertainty in the position evaluation of the abrasive particles, leading to exiguous fluctuations and irregularities despite the high number of detected abrasive particles. The standard deviation remains fairly constant over the radial position, what indicates that abrasive particles with different sizes remain randomly distributed within the AWJ.

### 3.5 Data comparison

Since the velocity and the abrasive particle distributions of all sets measured look very similar, the 14 different sets were plotted in Fig. 8 using dimensionless variables. The mass flow ratio was formed as the quotient of the abrasive particle mass flow rate and the water mass flow rate. The error bars indicate the standard deviation of the mean abrasive particle velocity.

The additional data in Fig. 8 were presented by Henning et al. (2011). They used a rotary disk anemometer introduced by Isobe et al. (1988) and optimized by Liu et al. (1999) to evaluate the mean velocity of an AWJ. The diagram in the right bottom corner of Fig. 8 shows the total data from Henning et al. (2011), including a linear fit and the calculated theoretical maximum. The narrow range of mass flow ratio from 0.1 to 0.2 actually justifies linear fitting. As expected, the velocity decreases slightly with increasing abrasive mass flow ratio.

Different AWJ cutting head geometries, a smaller orifice diameter and focusing tube diameter, and unknown abrasive particle size and type lead to the offset of about +12 % compared with the data acquired in the present work. Another important point is the fact that the rotary disk anemometer is biased to higher velocities, since low

**Fig. 7** Abrasive particle averaged velocity distribution within the AWJ of 39,217 abrasive particles detected at a water pressure of 91.0 MPa and a mass flow ratio of 0.183
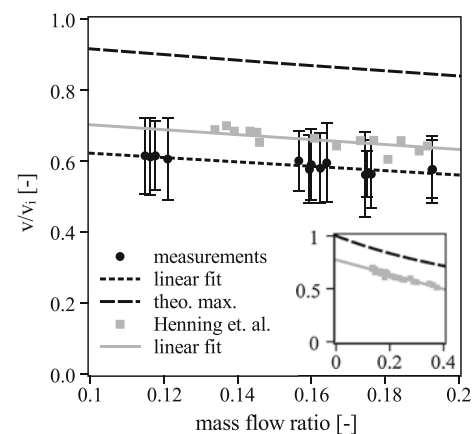
**Fig. 8** Abrasive particle mean velocity with varying mass flow ratios; comparison is made with data from Henning et al. (2011) and the theoretical maximum

velocities cannot induce erosion marks on the rotating disk (depending on disk material, for further information, see Liu et al. (1999)), and with higher mass flow ratios, water droplet and abrasive particle erosions are more difficult to distinguish.

To calculate the theoretical maximum velocity by momentum exchange as in Roth, et al. (2005), it is assumed that the abrasive particles and the water jet velocity are identical. The theoretical maximum is calculated as

$$v_{t,\max} = \frac{\dot{m}_{w,\text{in}} \cdot v_i}{\dot{m}_{w,\text{out}} + \dot{m}_{a,\text{out}}} \tag{3}$$

The air mass flow and the inlet velocity of the abrasive particles are neglected as well. The resulting curve shows the limiting value for the abrasive particle velocity.

### 3.6 Data overview

Table 1 in the "Appendix" shows all results evaluated with the corresponding AWJ parameters. Besides water pressure and mass flow rate, the number of detected abrasive particles, the mean axial velocity with the corresponding standard deviation of the abrasive particles, and all curve fit parameters including the coefficient of determination are given in the table. The Gauss parameters shown from the figures in Sects. 3.2, 3.3 and the "Appendix" are given by the Gauss function

$$f(x) = y_0 + A \cdot \frac{\sqrt{2/\pi}}{w} \cdot e^{-2 \cdot \left(\frac{x - x_c}{w}\right)^2} \tag{4}$$

The parameters for the polynomial fit from the figures in Sect. 3.4 and the "Appendix" are given as follows:

$$f(x) = a_0 + a_1 \cdot x + a_2 \cdot x^2 + a_3 \cdot x^3 \tag{5}$$

The standard deviation intervals are shown for the mean relative water pressure $\Delta p$ and the mean axial velocity $v$. Since for statistical reasons several parameter combinations were applied in experiments more than once, the number $N$ of abrasive particles evaluated vary strongly over the parameter combinations.

## 4 Conclusions and outlook

This paper shows that ultra-fast X-ray imaging is feasible for three-phase flow with spatial resolution below 100 μm. Abrasive particle distributions and velocities in AWJ can be extracted from the radiographic projections, in spite of the limited photon statistics at over 10 kHz frame rates and 5 μs inter-frame time. The measurements evaluated show a Gaussian distribution of the abrasive particles velocity downstream the focusing tube exit, a Gaussian distribution of the spatial position of the abrasive particles, and an almost flat spatial velocity distribution of the abrasive particles within the AWJ.

The spatial resolution in this work is sufficient to reliably track particles larger than about 100 μm in diameter. These represent more than 97 % of the initial particles entering the AWJ. The abrasive particles break up as a consequence of contact with the water jet and the focusing tube wall; this effect modifies the size distribution, increasing significantly the fraction of particles smaller than 100 μm. For the detection of these smaller particles, a higher spatial resolution must be chosen. Since the limiting factor is the photon flux rather than the detector pixel size, there are perspectives to achieve such conditions at new synchrotron sources. In such a way, the uncertainty of the observed average velocity (mainly due to the theoretically faster small particles that are not detected) can be minimized.

## Appendix

See Table 1, Figs. 9, 10 and 11.

**Table 1** Data overview

| # | $\Delta p$ [MPa] | $\dot{m}_a/\dot{m}_w$ | $N$ | $v/v_i$ | $R_v^2$ | $f_v(x)$ Parameters $A/x_c/w/y_0$ [-] | $R_s^2$ | $f_s(x)$ Parameters $A/x_c/w/y_0$ [-] | $R_p^2$ | $f_p(x)$ Parameters $a_0/a_1/a_2/a_3$ [-] |
|---|---|---|---|---|---|---|---|---|---|---|
| 1 | 91.1 ± 2.8 | 0.196 | 50,251 | 0.561 ± 0.119 | 0.994 | 1.00E+00 | 0.997 | 3.12E+00 | 0.974 | 5.70E−01 |
| | | | | | | 5.43E−01 | | −2.64E−03 | | −1.54E−05 |
| | | | | | | 1.39E−01 | | 1.41E+00 | | −2.20E−02 |
| | | | | | | 7.79E−02 | | 3.16E−03 | | −1.58E−03 |
| 2 | 91.0 ± 2.8 | 0.183 | 39,217 | 0.594 ± 0.111 | 0.995 | 1.00E+00 | 0.996 | 3.13E+00 | 0.952 | 6.00E−01 |
| | | | | | | 5.83E−01 | | −1.29E−03 | | −1.51E−03 |
| | | | | | | 1.52E−01 | | 1.41E+00 | | −2.01E−02 |
| | | | | | | 9.24E−02 | | 9.60E−04 | | 3.40E−05 |

**Table 1** continued

| # | $\Delta p$ [MPa] | $\dot{m}_a/\dot{m}_w$ | $N$ | $v/v_i$ | $R_v^2$ | $f_v(x)$ Parameters $A/x_c/w/y_0$ [-] | $R_s^2$ | $f_s(x)$ Parameters $A/x_c/w/y_0$ [-] | $R_p^2$ | $f_p(x)$ Parameters $a_0/a_1/a_2/a_3$ [-] |
|---|---|---|---|---|---|---|---|---|---|---|
| 3 | $142.8 \pm 3.1$ | 0.131 | 26,508 | $0.615 \pm 0.107$ | 0.997 | 1.00E+00 | 0.994 | 3.13E+00 | 0.982 | 6.22E−01 |
|   |   |   |   |   |   | 6.04E−01 |   | −8.62E−03 |   | −1.78E−03 |
|   |   |   |   |   |   | 1.40E−01 |   | 1.39E+00 |   | −2.33E−02 |
|   |   |   |   |   |   | 9.41E−02 |   | −3.25E−03 |   | −4.14E−03 |
| 4 | $143.0 \pm 3.1$ | 0.178 | 37,290 | $0.579 \pm 0.099$ | 0.994 | 1.00E+00 | 0.991 | 3.12E+00 | 0.914 | 5.86E−01 |
|   |   |   |   |   |   | 5.64E−01 |   | 4.27E−03 |   | 3.37E−03 |
|   |   |   |   |   |   | 1.34E−01 |   | 1.40E+00 |   | −1.99E−02 |
|   |   |   |   |   |   | 9.10E−02 |   | −7.06E−03 |   | −6.87E−03 |
| 5 | $143.0 \pm 3.1$ | 0.193 | 48,342 | $0.563 \pm 0.065$ | 0.996 | 1.00E+00 | 0.992 | 3.13E+00 | 0.934 | 5.70E−01 |
|   |   |   |   |   |   | 5.49E−01 |   | 7.83E−03 |   | 1.91E−03 |
|   |   |   |   |   |   | 1.32E−01 |   | 1.41E+00 |   | −2.27E−02 |
|   |   |   |   |   |   | 9.33E−02 |   | −1.13E−02 |   | −2.21E−03 |
| 6 | $194.8 \pm 3.8$ | 0.131 | 21,463 | $0.611 \pm 0.108$ | 0.996 | 1.00E+00 | 0.990 | 3.13E+00 | 0.908 | 6.17E−01 |
|   |   |   |   |   |   | 6.05E−01 |   | 6.44E−03 |   | −1.30E−03 |
|   |   |   |   |   |   | 1.42E−01 |   | 1.44E+00 |   | −1.33E−02 |
|   |   |   |   |   |   | 1.13E−01 |   | −4.56E−03 |   | 1.46E−05 |
| 7 | $195.2 \pm 3.6$ | 0.174 | 31,362 | $0.577 \pm 0.097$ | 0.996 | 1.00E+00 | 0.991 | 3.13E+00 | 0.991 | 5.83E−01 |
|   |   |   |   |   |   | 5.64E−01 |   | 1.42E−02 |   | 4.33E−03 |
|   |   |   |   |   |   | 1.35E−01 |   | 1.42E+00 |   | −2.24E−02 |
|   |   |   |   |   |   | 9.72E−02 |   | −8.23E−03 |   | −5.47E−03 |
| 8 | $195.1 \pm 3.7$ | 0.196 | 35,272 | $0.563 \pm 0.094$ | 0.997 | 1.00E+00 | 0.991 | 3.13E+00 | 0.947 | 5.69E−01 |
|   |   |   |   |   |   | 5.51E−01 |   | 1.11E−02 |   | 2.00E−03 |
|   |   |   |   |   |   | 1.30E−01 |   | 1.43E+00 |   | −1.89E−02 |
|   |   |   |   |   |   | 9.80E−02 |   | −9.58E−03 |   | −1.13E−03 |
| 9 | $296.5 \pm 5.2$ | 0.130 | 11,250 | $0.615 \pm 0.099$ | 0.995 | 1.00E+00 | 0.989 | 3.12E+00 | 0.936 | 6.34E−01 |
|   |   |   |   |   |   | 6.19E−01 |   | −7.37E−05 |   | 8.14E−03 |
|   |   |   |   |   |   | 1.32E−01 |   | 1.45E+00 |   | −1.80E−02 |
|   |   |   |   |   |   | 1.90E−01 |   | 6.60E−03 |   | −9.13E−03 |
| 10 | $296.7 \pm 5.0$ | 0.171 | 40,358 | $0.600 \pm 0.085$ | 0.998 | 1.00E+00 | 0.982 | 3.13E+00 | 0.962 | 6.05E−01 |
|   |   |   |   |   |   | 5.92E−01 |   | 4.07E−03 |   | 3.90E−03 |
|   |   |   |   |   |   | 1.26E−01 |   | 1.51E+00 |   | −1.64E−02 |
|   |   |   |   |   |   | 6.07E−02 |   | −3.34E−02 |   | −5.53E−03 |
| 11 | $296.6 \pm 5.0$ | 0.208 | 48,810 | $0.577 \pm 0.082$ | 0.998 | 1.00E+00 | 0.988 | 3.12E+00 | 0.919 | 5.85E−01 |
|   |   |   |   |   |   | 5.72E−01 |   | −2.51E−03 |   | 3.59E−03 |
|   |   |   |   |   |   | 1.25E−01 |   | 1.52E+00 |   | −1.63E−02 |
|   |   |   |   |   |   | 7.26E−02 |   | −3.19E−02 |   | −4.07E−03 |
| 12 | $355.0 \pm 4.8$ | 0.132 | 23,314 | $0.606 \pm 0.115$ | 0.992 | 1.00E+00 | 0.977 | 3.13E+00 | 0.974 | 6.15E−01 |
|   |   |   |   |   |   | 6.20E−01 |   | 2.14E−03 |   | 1.26E−02 |
|   |   |   |   |   |   | 1.13E−01 |   | 1.63E+00 |   | −1.60E−02 |
|   |   |   |   |   |   | 1.74E−01 |   | −4.44E−02 |   | −2.21E−03 |
| 13 | $355.3 \pm 4.7$ | 0.174 | 31,877 | $0.590 \pm 0.100$ | 0.997 | 1.00E+00 | 0.980 | 3.13E+00 | 0.947 | 5.97E−01 |
|   |   |   |   |   |   | 5.94E−01 |   | −2.22E−02 |   | 5.42E−03 |
|   |   |   |   |   |   | 1.22E−01 |   | 1.62E+00 |   | −1.59E−02 |
|   |   |   |   |   |   | 1.05E−01 |   | −4.67E−02 |   | 2.99E−03 |
| 14 | $354.9 \pm 4.6$ | 0.212 | 36,726 | $0.576 \pm 0.094$ | 0.997 | 1.00E+00 | 0.973 | 3.13E+00 | 0.912 | 5.84E−01 |
|   |   |   |   |   |   | 5.76E−01 |   | −1.61E−02 |   | 4.08E−03 |
|   |   |   |   |   |   | 1.22E−01 |   | 1.65E+00 |   | −1.56E−02 |
|   |   |   |   |   |   | 8.86E−02 |   | −5.19E−02 |   | −1.24E−04 |

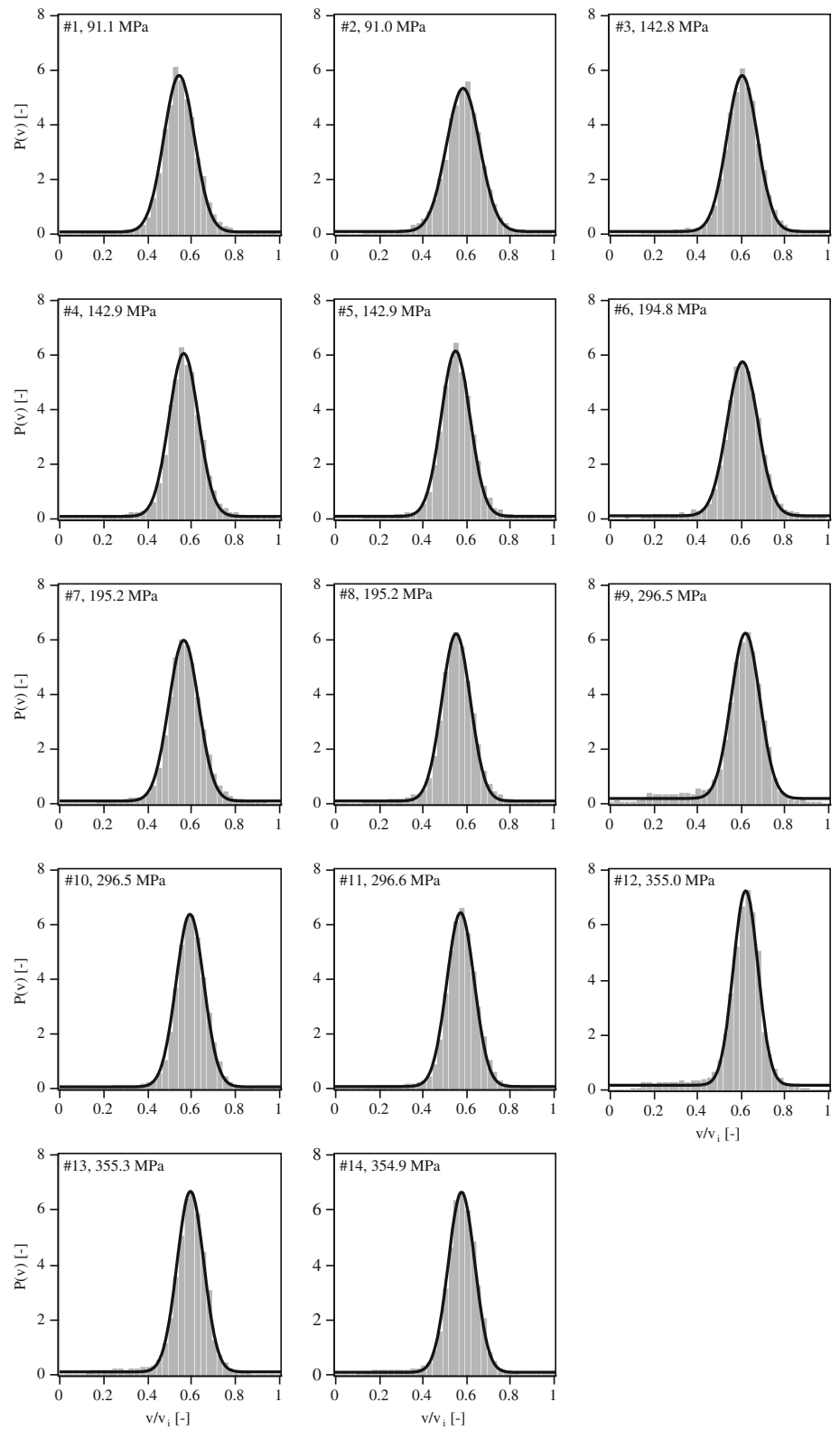**Fig. 9** Abrasive particle velocity distributions of all measured sets

**Fig. 10** Abrasive particle distribution within the AWJ of all measured sets
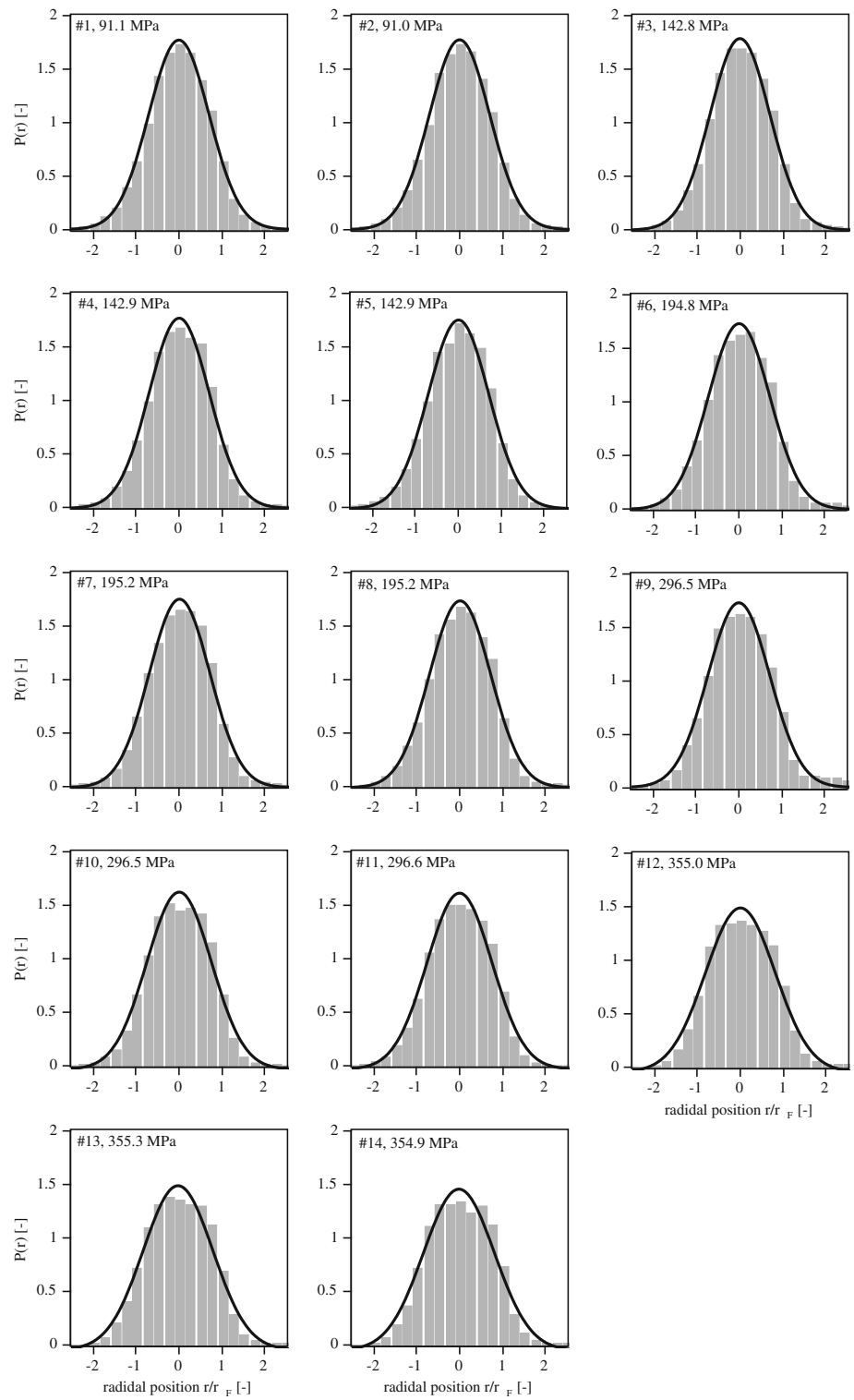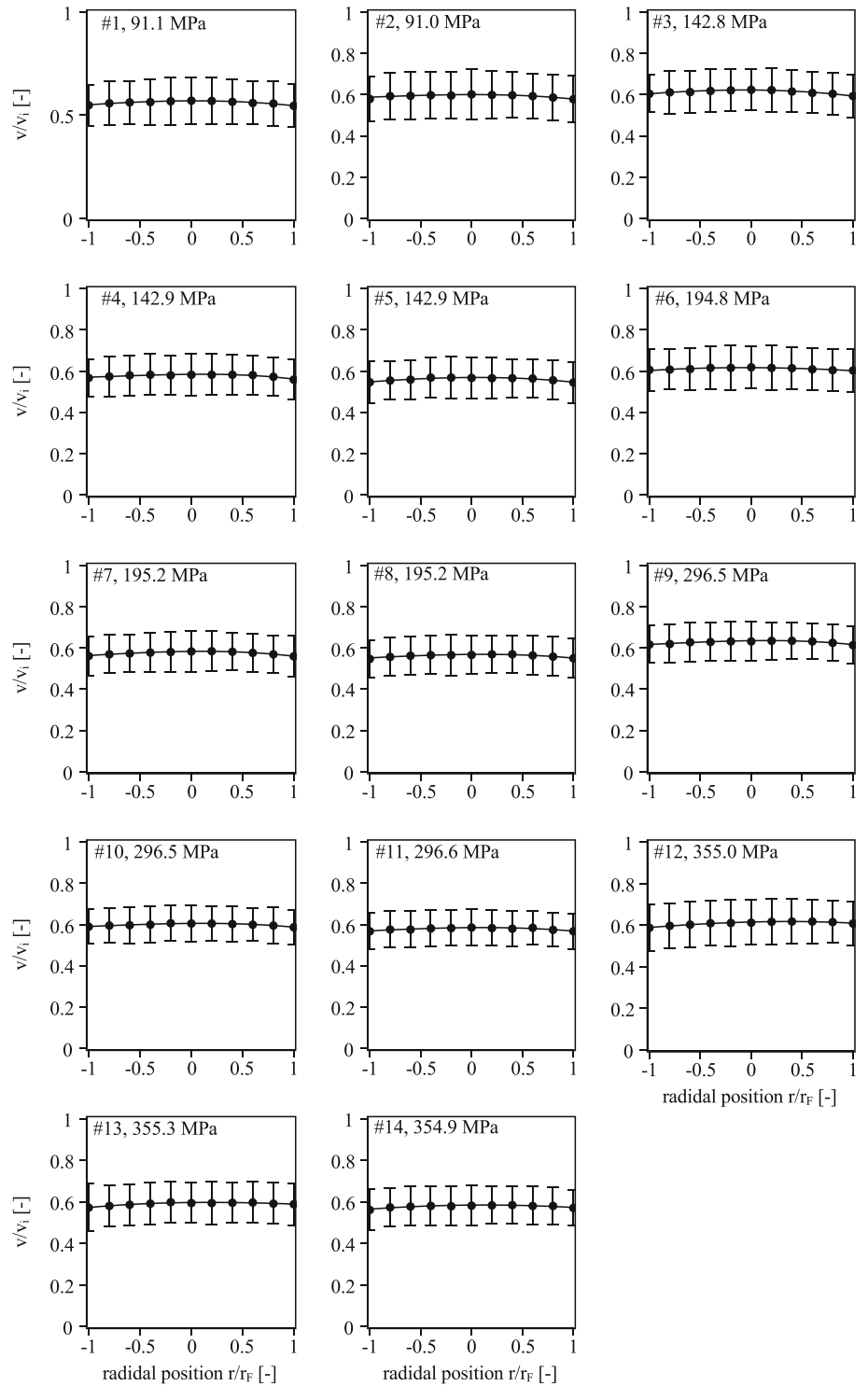
**Fig. 11** Abrasive particle averaged velocity distribution within the AWJ of all measured sets

# References

Balz R, Heiniger KC, (2011) Determination of spatial velocity distributions of abrasive particles in abrasive water jets using laser-inuced fluorescence under real conditions. Proceedings of 16th WJTA-IMCA Conference and Expo

Bieberle M, Fischer F, Schleicher E, Koch D, Menz H-J, Mayer H-G, Hampel U (2009) Experimental two-phase flow measurement using ultra fast limited-angle-type electron beam X-ray computed tomography. Exp Fluids 47:369–378. doi:10.1007/s00348-009-0617-6

Chen W-L, Geskin ES, (1997) Correlation between particle velocity and conditions of abrasive waterjet formation. Proceedings of 6th American water jet conference

Claude X, Merlen A, Thery B, Gatti O (1998) Abrasive waterjet velocity measurements. Proceedings of 14th International Conference on Jetting Technology, p 235 ff

Geskin ES, Chen WL, Chen SS, Hu F, Khan MEH, Kim S (1989) Investigation of anatomy of an abrasive waterjet. Proceedings of 5th American water jet conference, pp 217–230

Hansson RC, Park HS, Dinh T-N (2009) Simultaneous high speed digital cinematographic and X-ray radiographic imaging of a intense multi-fluid interaction with rapid phase changes. Exp Therm Fluid Sci 33:754–763. doi:10.1016/j.expthermflusci.2009.01.011

Hashish M (2003) Inside AWJ nozzles. Proceedings of 12th WJTA conference, 17–19 08, pp 1-D

Henning A, Miles P, Stang D (2011) Efficient operation of abrasive waterjet cutting in industrial applications. Proceedings of 16th WJTA-IMCA conference and Expo

Hlavac LM, Sosnovec L, Martinec P (1999) Abrasive for high energy water jet: investigation of properties. Proceedings of 10th WJTA conference, pp 409–418

Isobe T, Yoshida H, Nishi K (1988) Distribution of abrasive particles in abrasive water jet and acceleration mechanism. Proceedings of 9th international symposium on jet cutting technology

Lee SJ, Kim S (2005) Simultaneous measurement of size and velocity of microbubbles moving in an opaque tube using an X-ray particle tracking velocimetry technique. Exp Fluids 39:490–495. doi:10.1007/s00348-005-0956-x

Li HY, Geskin ES, Chen WL (1989) Investigation of forces exerted by an abrasive water jet on a workpiece. Proceedings of 5th American water jet conference

Lim JS (1990) Two-dimensional signal and image processing. Prentice Hall, Englewood Cliffs

Liu H-T, Miles PJ, Cooksey N, Hibbard C (1999) Measurements of water-droplet and abrasive speeds in a ultrahigh-pressure abrasive-waterjets. Proceedings of 10th American waterjet conference

Neusen KF, Alberts DG, Gores TJ, Labus TJ (1990) Distribution of mass in a three-phase abrasive waterjet using scanning X-ray densitometry. Proceedings of 10th international symposium on jet cutting technology

Neusen KF, Gores TJ, Amano RS (1994) Axial variation of article and drop velocities downstream from an abrasive water jet mixing tube. Proceedings of 12th international conference on jet cutting technology

Osman AH, Mabrouki T, Théry B, Buisine D (2004) Experimental analysis of high-speed air-water jet flow in an abrasive water jet mixing tube. Flow Meas Instrum (15):37–48

Ramirez AI, Som S, Aggarwal SK, Kastengren AL, El-Hannouny EM, Longman DE, Powell CF (2009) Quantitative X-ray measurements of high-pressure fuel sprays from a production heavy duty diesel injector. Exp Fluids 47:119–134. doi:10.1007/s00348-009-0643-4

Roth P, Looser H, Heiniger KC, Bühler S (2005) Determination of abraive particle velocity using laser-induced fluorescence and particle tracking methods in abrasive water jets. Proceedings ot 13th American waterjet conference

Swanson RK, Kilman M, Cerwin S, Tarver W (1987) Study of particle velocities in water driven abrasive jet cutting. Proceedings of 4th U.S. water jet conference, pp 103–108

Wang Y, Liu X, Im KS, Lee WK, Wang J, Fezzaa K, Hung DLS, Winkelman JR et al (2008) Ultrafast X-ray study of dense-liquid-jet flow dynamics using structure-tracking velocimetry. Nat Phys 4:305–309